Indium – Polycarboxylic Acid Ligand Interactions Modify InP Quantum Dot Nucleation and Growth

Helen Larson and Brandi M. Cossairt*

Department of Chemistry, University of Washington, Seattle, WA 98195, United States

*cossairt@uw.edu

Abstract

Size control through precursor reactivity in InP quantum dot (QD) synthesis has been difficult due to the presence of kinetically persistent InP clusters when using conventional indium carboxylate and tris(trimethylsilyl)phosphine chemistry. However, the advent of the indium halide/aminophosphine-based synthesis creates new opportunities to harness precursor design to impact nucleation and growth. Driven to further explore indium coordination as a synthetic handle in InP QD synthesis, we have examined the effect of a strongly chelating anion on the nucleation and growth of InP QDs. Increasing the equivalents of metal-chelating aminopolycarboxylic acid EDTA ($[CH_2N(CH_2CO_2H)_2]_2$) (0 to 0.75 equivalents per indium) is found to decrease the final diameter of InP QDs from 4.5 to 2.3 nm by lowering the initial InP growth rate. This size trend is rationalized by invoking a continuous nucleation model. Control experiments carried out with substoichiometric equivalents of indium do not exhibit a drastic size decrease, pointing to complex effects of EDTA on indium precursor reactivity. By ^{1}H NMR spectroscopy, EDTA is identified to form an octahedral complex with indium that is less reactive. This competitive decrease in reactivity and in the effective concentration of indium precursor is proposed to suppress the initial InP growth rates and consequently decrease the final size of the nanocrystals.

Introduction

Morphological control over nanomaterials by leveraging the interplay of organic and inorganic components is a central focus in the colloidal synthesis community. Nature has also developed exquisite mechanisms for controlling crystal growth at the nanoscale to produce hierarchically structured organic-inorganic composites, like shells and bone. Despite this, the connection between colloidal nanomaterial synthesis and the field of biomineralization is underexplored. A review from Nudelman and Sommerdijk details how the elements of chemical, spatial, structural, morphological, and constructional control in biomineralization systems apply to materials chemistry.[1] Molecular or macromolecular templates with specific binding groups or enclosed spaces regulate the location, reactivity, and concentration of mineral precursors that control nucleation and growth of minerals to impact their shape, size, phase, and assembly. Application of biomineralization design principles has inspired complex synthetic inorganic nanomaterials. Biomimetic macromolecules can template hybrid hierarchical inorganic materials,[2–7] and molecular templates designed to bind certain crystal facets can control the

nucleation and growth of inorganic nanomaterials.[8–12] The quantum dot (QD) community can learn from nature's lessons on biomineralization to unlock new synthetic paradigms.

A promising avenue to introduce biomineralization principles to colloidal quantum dot synthesis is to position the capping ligand to take on a more complex cation templating role. Commercially available aminopolycarboxylic acids contain multiple functional groups that mimic the organized binding groups seen in natural mineralization templates such as peptides, and in particular ethylenediaminetetraacetic acid (EDTA) is cheap, low toxicity, and known to chelate metal ions.[13] In the literature, polycarboxylic acids have been shown to control the nucleation and growth of metal oxide and rare-earth fluoride nanomaterials.[14–22] While the use of EDTA as an additive in colloidal semiconductor synthesis is rare, there is precedent for EDTA interacting with metal ions during colloidal synthesis. The strong metal ion chelation of EDTA has been seen to prevent premature nucleation during heating,[15] lower reactivity and prevent undesirable side reactions,[16,18] and sequester metal ions during growth to inhibit excessive nucleation to control particle size.[14] A study of CdS microparticles by Sugimoto and coworkers showed that nucleation was controlled by the molar ratio of EDTA to the cadmium precursor which in turn controls the Cd^{2+} available for nucleation, and then the Cd–EDTA complexes slowly release Cd^{2+} for monodisperse growth.[14]

Precursor identity has been a long standing tool to affect QD synthesis, where precursor reactivities balance nucleation and growth to offer uniform, size-controlled samples.[23,24] This study uses InP QD synthesis to explore the intersections of biomineralization-inspired metal ion control and colloidal QD precursor reactivity. Despite the promise of InP as a leading less toxic, commercially viable semiconductor, realizing precursor conversion reactivity controlled InP QD synthesis has been challenging. For InP QDs made using indium carboxylates and tris(trimethylsilyl)phosphine, kinetically trapped magic sized cluster intermediates complicate control through precursor reactivity, and existing efforts mainly focus on tuning phosphorus reactivity.[25–27] There have been few examples to date of using indium chemistry to control the synthesis of InP QDs despite a promising theoretical study that highlights the importance of the indium-oxygen bond cleavage energetics in InP bond formation using indium carboxylates.[28,29] Importantly, the advent of indium halides and aminophosphines as precursors for InP QDs opens up new avenues for precursor conversion reactivity control due to the avoidance of kinetic traps like the magic sized cluster.[30–34] Varying the halide in the indium precursor tunes the final size of the QDs,[30,31] and aminophosphines of different reactivities have been employed to effect precursor conversion reactivity control.[32,33] In particular, recent work identifies a continuous nucleation and size-focusing growth mechanism for InP QDs grown using the aminophosphine chemistry, which allows for in depth interpretation of precursor reactivity effects.[32]

Here we investigate the effect of aminopolycarboxylic acid EDTA on the nucleation and growth of InP QDs made using indium chloride and tris(diethyl)aminophosphine. By varying the equivalents of EDTA per indium, we identify an EDTA-dependent trend in the final QD size. Analysis of the initial InP growth rates using UV-vis absorbance spectra of reaction aliquots and rationalization through a continuous nucleation mechanism explains the size trend. Specific indium – EDTA interactions are investigated through ^{1}H NMR spectroscopy and an octahedral indium EDTA complex is identified with low reactivity. We demonstrate how EDTA dose-dependent size control of InP QDs is achieved through a chelation-induced indium sequestration

pathway. We present EDTA as an indium precursor modifier that expands the accessible QD size range of a given indium halide.

Results and Discussion

Previous studies have optimized the synthesis conditions for making InP QDs using aminophosphines, including indium concentration and equivalents of aminophosphine relative to the indium halide (**Scheme 1**).[31] The reaction temperature of 180 °C for this study was chosen to both be comparable to literature precedent and avoid the decomposition of EDTA, which interferes with InP formation at temperatures above 180 °C (**Figure S1**).[35] The primary indium halide used is indium chloride to offer the largest window for size control, because as the worst leaving group out of the halide series (*i.e.*, chloride, bromide, and iodide) it facilitates the formation of the largest QDs. Consistent results are also obtained with indium iodide (see Supporting Information).

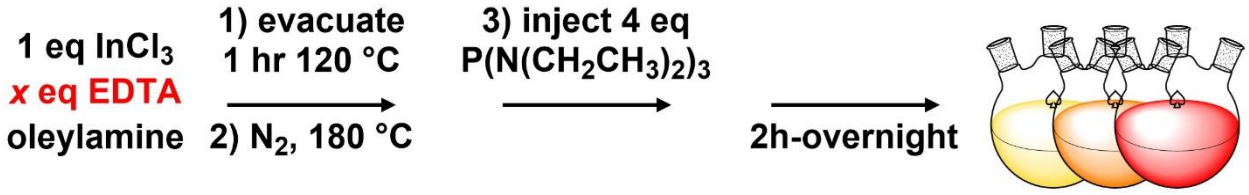

Scheme 1. Aminophosphine-based InP QD synthesis with ethylenediaminetetraacetic acid (EDTA) additive (x = 0, 0.25, 0.5, 0.75).

Increasing the dose of EDTA from 0 to 0.75 equivalents per indium controls the final size of InP QDs as evidenced by a range of lowest energy electronic transitions (LEET) from ~590 to ~400 nm in UV-vis absorbance data (**Figure 1a**). Fitting the low energy tail of each final absorbance spectrum to a gaussian peak to approximate the excitonic absorbance transition gives LEETs at 583, 558, 510 nm for 0, 0.25, and 0.5 equivalents of EDTA per indium, respectively. The approximate LEET for the InP QDs made with 0.75 equivalents of EDTA is estimated using a Tauc plot to be 393 nm (method in SI). Transmission electron microscopy (TEM) images reveal a slight morphology change from spherical to a truncated tetrahedral nanocrystal shape as well as a size increase as the equivalents of EDTA decrease (**Figure 1c-f**). The nanocrystal size can be estimated from the LEET based off electron confinement and effects of shape.[36] Due to stronger confinement in a tetrahedral nanocrystal, the upper size estimate for QDs with LEETs of 583, 558, 510, and 393 nm are edge lengths of 5.9, 5.2, 4.2, and 2.4 nm while assuming a spherical nanocrystal gives diameters of 3.2, 3, 2.6, and 1.8 nm, respectively. The measured diameters from TEM images are 4.5 ± 0.6, 4.2 ± 0.8, 3.9 ± 0.6, and 2.3 ± 0.8 nm for syntheses using 0, 0.25, 0.5, and 0.75 equivalents of EDTA, respectively, agreeing with the identified morphology change from small spheres to larger tetrahedra (**Figure S2, S3**).

Powder X-Ray Diffraction (pXRD) data of the purified QDs show zinc blende phase InP (**Figure 1b**). Scherrer analysis was performed on the pXRD patterns with defined zinc blende peaks and confirms the size trend with average crystallite sizes of 3.5 ± 0.3 and 2.8 ± 0.4 nm for InP QDs made with 0 and 0.25 equivalents of EDTA, respectively. We note that the smaller QD samples have broad diffraction patterns as is typical of nanocrystals of that size.[37] Additionally,

analysis of the peak centered at 20 degrees two theta, which is attributed to the ordering of the surface ligands, offers insight into the size and composition of the QDs. Calvin and coworkers have recently shown through experimental diffraction patterns and theoretical models of different sized InP QDs that the peak from ligand ordering increases in relative intensity compared to the lowest index zinc blende peak as the nanocrystal size decreases.[38] The diffraction patterns were fit to gaussian peaks to confirm that this ratio increases for the size decrease observed across the EDTA series (**Figure S4**).

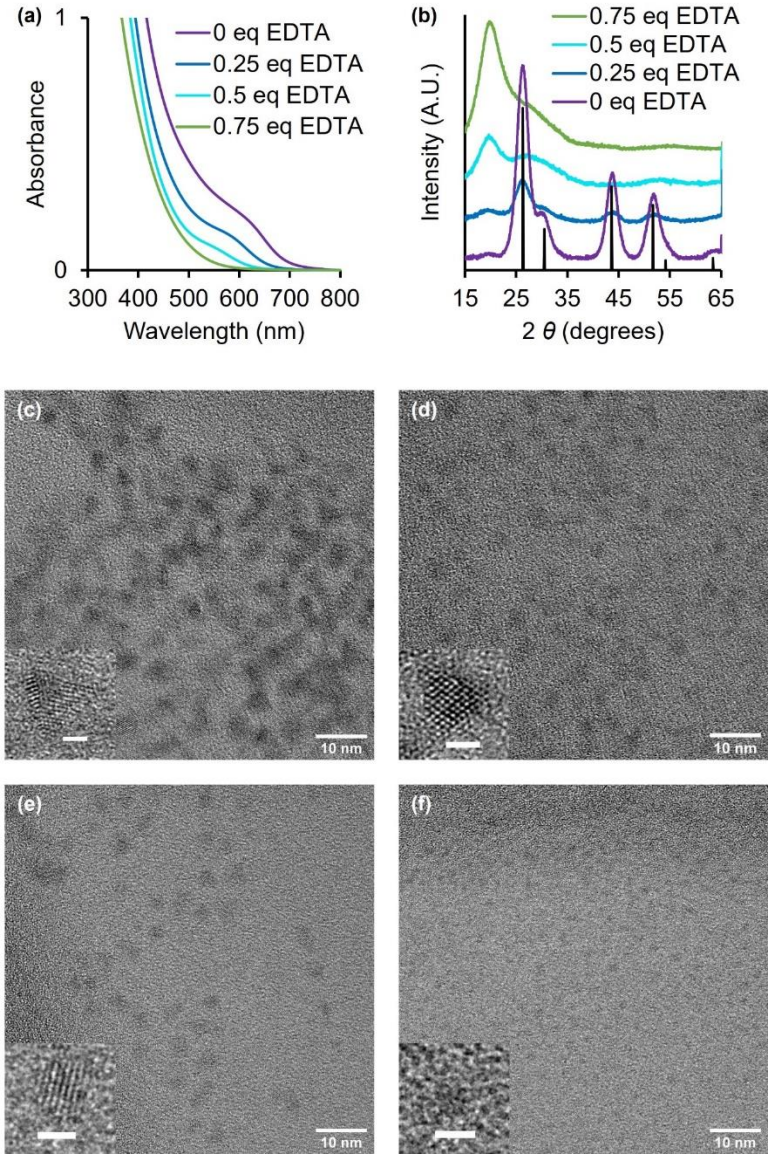

Figure 1. (**a**) Overlay of absorbance spectra of final reaction aliquots of InP QDs made using varying equivalents of EDTA per indium. (**b**) XRD pattern of InP QDs after purification to remove excess ligand. TEM images of InP QDs made using (**c**) 0, (**d**) 0.25, (**e**) 0.5, and (**f**) 0.75 equivalents of EDTA, with diameters 4.5 ± 0.6 nm, 4.2 ± 0.8 nm, 3.9 ± 0.6 nm, and 2.3 ± 0.8 nm, respectively. Insets (c-f) show representative QD morphology (scale bars are 2 nm).

There are two options for how EDTA could be impacting the nucleation and/or growth processes to cause the size control effect. The first is surface binding, which would stabilize the surface and impede nanocrystal growth.[21] The second is interference with the precursor conversion reaction, which would affect the balance between nucleation and growth.[14,32,33] Considering the first option, the observed size trend is consistent with increasing equivalents of EDTA acting as a strong indium chelating ligand, stabilizing the surface and decreasing the QD diameter until growth is prevented entirely. For this hypothesis to be likely, EDTA would be expected to be found on the surface of the QDs after purification as one of the capping ligands. However, by ^{1}H NMR spectroscopy there is no identifiable surface bound EDTA present in the purified QD samples, only the expected oleylamine capping ligands are observed (**Figure S5**).[36,39] The broadening of the ligand resonances as the QD size decreases indicates an increase in ligand disorder caused by the morphology change from tetrahedral to quasi-spherical.[40] The broad resonances centered around 4.2 ppm that increase in intensity with more EDTA in the synthesis can be attributed to species from amine oxidation reactions such as imines and iminiums.[41] IR spectroscopy was taken of purified and dried samples of the QD series and the expected strong carboxylate stretch from EDTA was not identified in any of the spectra (**Figure S6**). Concluding that EDTA is not present on the surface to an extent that adequately explains the observed size control, we turned to the hypothesis that EDTA impacts precursor reactivity.

Recent work on the mechanism of InP nucleation and growth in the aminophosphine system gives great insights on how to interpret the size trend through perturbation of precursor conversion.[32,33] McMurtry and coworkers found that nucleation takes up a sizable fraction of the total reaction time, ranging from a half to less than a tenth of the reaction time.[32] At lower reaction temperatures, such as 180 °C used in the present study, nucleation of new nanocrystals occurs over about half of the reaction time. For aminophosphines of varying reactivities, the dependence of size on different initial growth rates was found to only become significant at higher temperatures. However, Valleix and coworkers separately observed a decreasing size trend by adding increasing equivalents of a diamine at a reaction temperature of 180 °C.[33] They proposed that a diethylaminophosphine – diamine complex forms from the transaminated oleylaminophosphine, which acts as a competitive reaction to InP production. The crucial point seems to be that the competitive phosphorus precursor reaction both decreases the amount of active phosphorus available to convert to InP *and* decreases the InP production rate. A control done with a lower molar amount of the initial aminophosphine did not decrease QD size, which shows that the lower rate of InP formation is crucial to the size control effect.

In this study, QD size decreases as equivalents of EDTA are increased, which is the same trend seen in the diamine dose-dependent size control study. To probe whether EDTA could be having a similar effect on indium availability as the diamine was found to have on phosphorus availability, we investigated initial rates. The initial rate of InP formation decreases with increasing equivalents of EDTA (**Figure 2a**). Initial rates based off absorbance increases in reaction aliquots are sometimes referred to as precursor conversion rates or monomer production rates. However, when the rate is calculated by attributing absorbance at high energy wavelengths to InP units using bulk zinc blende InP parameters, then it should more accurately be thought of as the initial growth rate of crystalline InP and not a measure of monomer production rate. Under the regime of burst nucleation, lower initial rates of monomer production cause less nuclei to

form and then those nuclei experience more surface growth due to the mass balance of monomers left over in solution after the nucleation event (**Figure 2c**).[23,24,27] In that scenario, low initial InP formation rates lead to larger QDs but this is the opposite to what is observed with the EDTA series. This can be rationalized by pointing to the evidence that InP made using aminophosphines undergoes continuous nucleation rather than a burst nucleation event.[32] During a longer nucleation period, lower initial InP growth rates could imply slower solute production leading to slower growth on existing nuclei (**Figure 2c**). Kinetics of initial InP growth and nucleation are likely affected similarly due to the redox reaction required for InP bond formation, which convolutes the identity of a monomer species and blurs the distinction between nucleation and surface growth. The extended nucleation period allows for many nuclei to form and grow slowly to be small QDs without loss of critical concentration when there are low initial InP formation rates. Similar logic follows that high initial growth rates lead to larger QDs. After the extended nucleation period, the QDs experience size dependent growth allowing for a monodisperse population.[32] This is observed in the current system by the narrowing of the full width at half maximum of the LEET in a representative InP QD synthesis using 0.25 equivalents of EDTA (**Figure S7**). The relative yield of InP is also seen to decrease with increasing equivalents of EDTA, which supports smaller QDs grown with lower initial rates (**Figure 2b**). Additionally, lower yields raise the option of precursor loss to some nonproductive route. With potential for initial rates to cause the observed size trend, we next examine the role of EDTA in perturbing the initial InP formation rates.

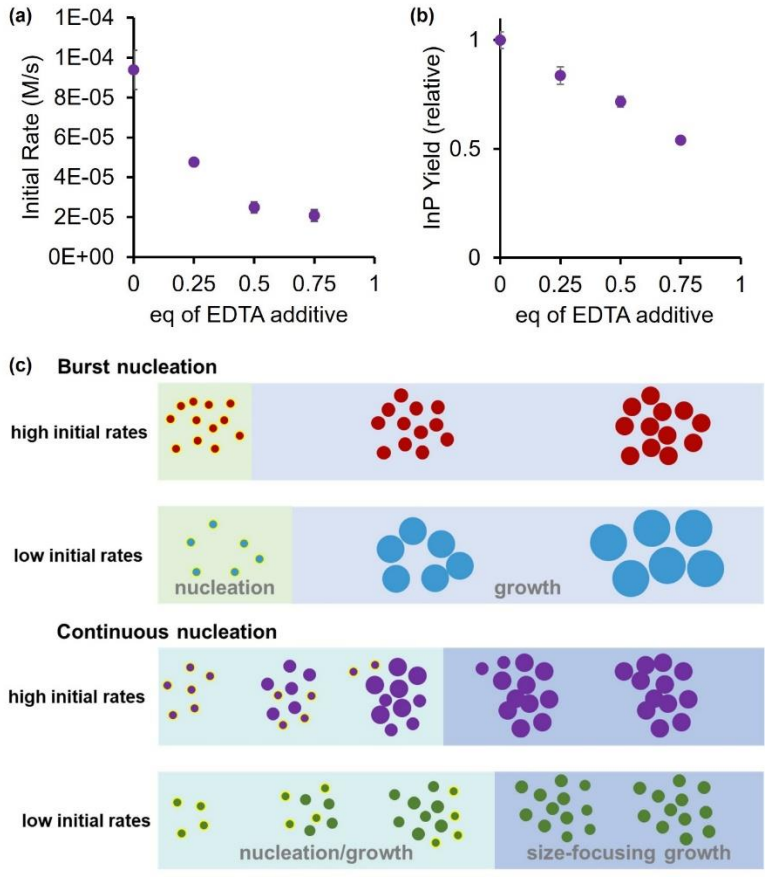

Figure 2. Initial rates of InP growth (**a**) and InP yield (**b**) for InP QDs made using varying equivalents of EDTA. (**c**) Scheme showing size dependence on initial rates during burst nucleation compared to continuous nucleation scenarios.

Due to its strong chelation to metal ions, it is possible that EDTA is simply sequestering indium cations, and the lower concentration and molar amount of indium in solution is causing smaller QDs to form. Syntheses with a reduced $InCl_3$ stoichiometry of 0.5 and 0.25 equivalents were run as a control to compare to the 0.5 and 0.75 equivalents of EDTA experiments, respectively. Fitting the final absorbance traces shows only a ~50 nm blueshift in the LEET when equivalents of $InCl_3$ are reduced from 1 to 0.25 (**Figure 3**) rather than the ~200 nm blueshift observed when using EDTA. The yields of the lower equivalents of $InCl_3$ syntheses decrease relative to the full stoichiometric equivalent as is expected for less indium (**Figure S8**). The role of EDTA in the system is more complex than complete sequestration because simply less indium in solution does not provide the same magnitude of size control. The initial rates of the control $InCl_3$ series also decrease with lower molar amounts added; however, the decrease is less than is seen with the corresponding EDTA equivalents (**Figure S9**). Coupled with the slight size decrease seen as the amount of $InCl_3$ decreases, this continues to point to an EDTA-specific effect on initial rates as the culprit for the observed size trend. Additionally, size control by varying the initial rates would be a kinetic effect and this can be confirmed by observing faster growth to larger QDs at higher temperatures. This was performed on the 0.75 equivalents of EDTA synthesis condition, and faster initial rates were observed as the temperature was increased up to 220 °C (**Figure 4**). However, the system becomes unstable above 180 °C after 1 hour (190 °C) or 20 minutes (220 °C) as evidenced by a decrease in absorbance at high energy wavelengths pointing to QD decomposition (**Figure S1**). EDTA is known to undergo thermal decomposition above 180 °C in aqueous conditions.[35]

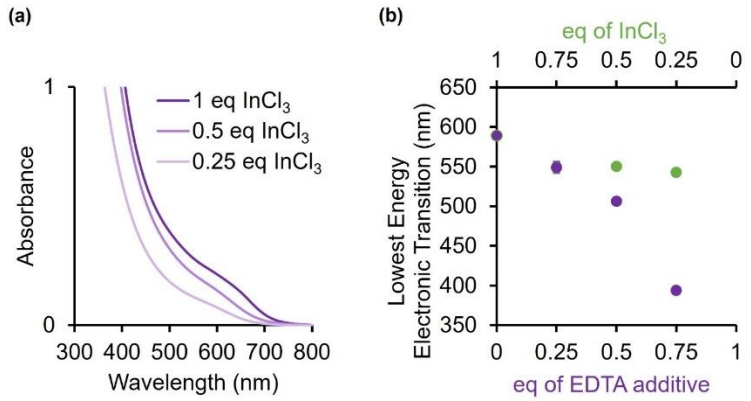

Figure 3. (**a**) Overlay of absorbance spectra of final reaction aliquots of InP QDs made using varying concentrations of $InCl_3$. (**b**) Comparison of the lowest energy electronic transitions between lower $InCl_3$ concentration and equivalents of EDTA additive.

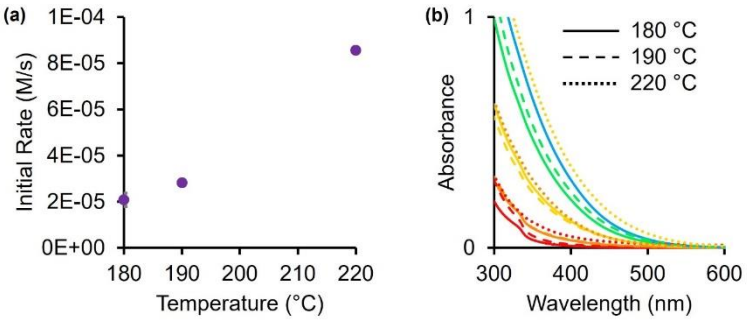

Figure 4. (**a**) Initial rates of InP growth increase for InP QDs made using 0.75 eq. EDTA with increasing reaction temperatures of 180, 190, and 220 °C. (**b**) Absorbance spectra of initial reaction aliquots (red 30 s, orange 2 min, yellow 5 min, green 10 min, blue 15 min) across the three reaction temperatures (180 °C solid, 190 °C dashed, 220 °C dotted) for InP QDs made using 0.75 eq. EDTA.

To rule out significant influences of EDTA on the phosphorus precursor chemistry, ^{31}P NMR spectroscopy was used to track molecular phosphorus byproducts.[31] Reaction aliquots of the InP QD synthesis using 0.75 equivalents of EDTA show the active transaminated aminophosphine species disappearing over early time points (~10 minutes) as well as the tautomer species of the active transaminated aminophosphines at 14 and 11 ppm as they convert back to the more active phosphorus precursor (**Figure 5**). The phosphonium salt byproduct of InP bond formation (30 ppm) appears over the first 10 minutes of the reaction accompanied by an increasing amount of an additional byproduct with a resonance at 18 ppm. This peak has been observed as a minor species in previous studies, but not nearly with the intensity seen here.[31,42] The amide-forming reaction between the carboxylic acids of EDTA and oleylamine produces water as a byproduct (observed by ^{1}H NMR in the absence of phosphorus in **Figure S10**), which taken alongside the chemical shift suggests an aminophosphine oxide.[43] There is excess unincorporated phosphorus in the reaction because of the lower InP yields with higher equivalents of EDTA, and the increasing amount of aminophosphine oxide serves as a reasonable outlet. The phosphonium salt byproduct is observed in the ^{31}P NMR spectra of the crude reactions before purification throughout the EDTA series, as well as increasing amounts of the resonance attributed to an aminophosphine oxide as the equivalents of EDTA increase from 0 to 0.5 per indium (**Figure S11**).

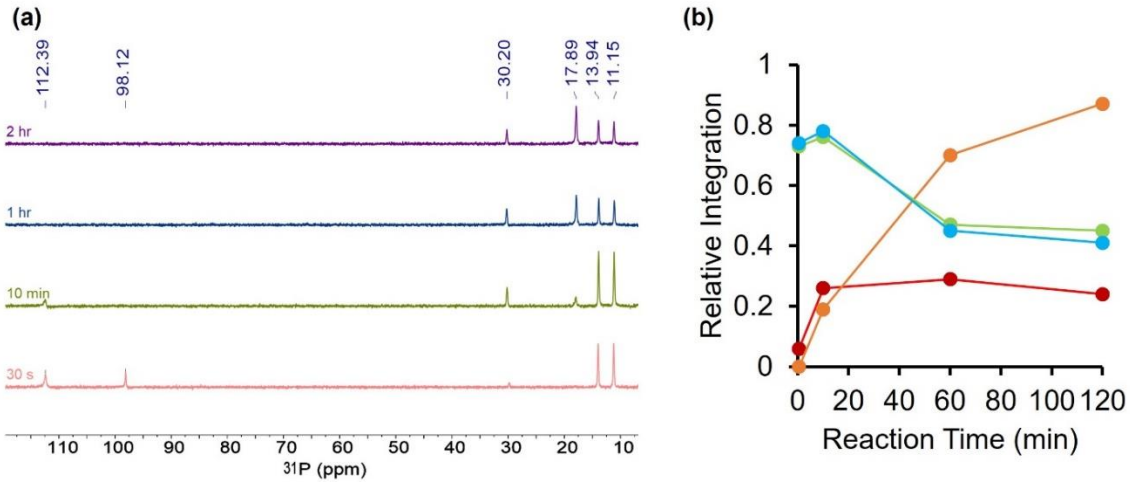

Figure 5. (**a**) ^{31}P NMR (benzene-d_6, 500 MHz, 298K) spectra of reaction aliquots of InP QDs made using 0.75 eq. EDTA. (**b**) Integrations of phosphonium salt (30 ppm, red), proposed aminophosphine oxide (18 ppm, orange), and tautomers of the active transaminated aminophosphine species (14, 11 ppm, green, blue).

EDTA was added to the InP QD synthesis for its multiple carboxylic acid functional groups to interact with the indium cations during InP nucleation and growth. The previous work using diamines to control phosphorus availability and reactivity pointed to a competitive precursor reaction as a means to lower initial rates and lead to size control.[33] A potential competitive precursor reaction could involve partial or full binding of EDTA to indium species in the reaction. EDTA is known to form pentagonal bipyramidal complexes with In^{3+} among a plethora of other metal cations in aqueous environments with water occupying the seventh coordination site.[13] However, there are few reports describing the interactions between EDTA and indium or similar metals in organic solvents, likely due to low solubilities at room temperature. To show that EDTA can make complexes with indium chloride in aprotic solvents assisted by amines, ^{1}H NMR spectroscopy was used to track the binding of EDTA to indium. To simulate the conditions of the initial reaction mixture before phosphorus addition, indium chloride and EDTA were reacted in equimolar amounts in deuterated dimethyl sulfoxide with four equivalents of oleylamine per indium. After allowing the mixture to stir overnight, the ^{1}H NMR spectrum shows an AB quartet with coupling $J_{H\text{-}H}$ of 16 Hz at 3.1 and 2.9 ppm with integrations of 4 protons each, a singlet around 2.7 ppm overlapping with the oleylamine alpha proton triplet with an integration for 4 protons, and resonances attributed to the oleylammonium protons (**Figure 6**).

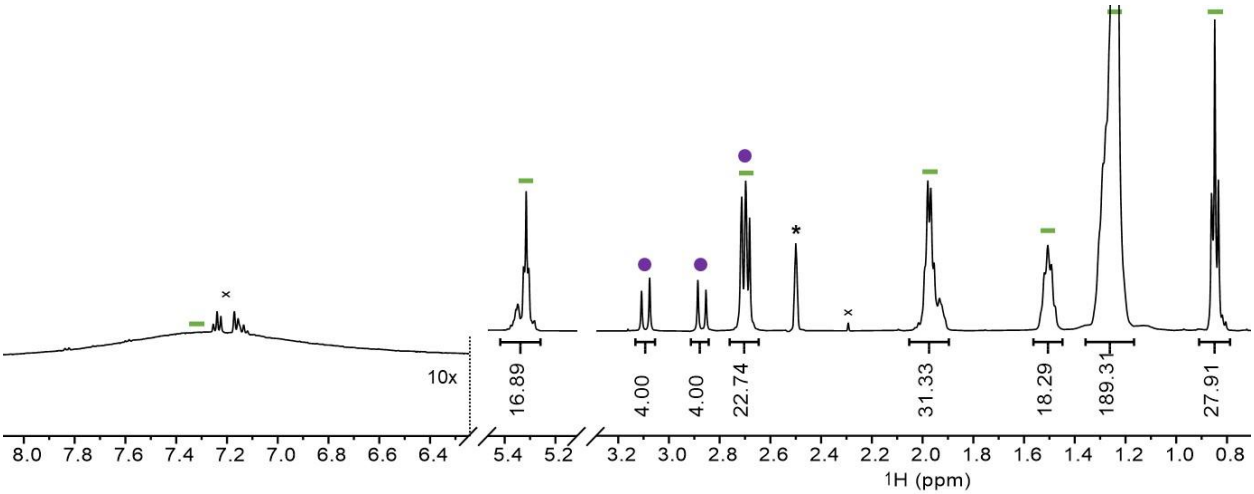

Figure 6. ^{1}H NMR (DMSO-d_6, 500 MHz, 298K) spectrum of 1 eq. $InCl_3$, 1 eq. EDTA, and 4 eq. oleylamine, with integrations for the methylene peaks of EDTA at 3.09 and 2.87 ppm (J_{HH} = 16 Hz). EDTA protons are labeled with purple circles, oleylamine protons are labeled with green dashes, and residual DMSO is at 2.50 ppm (*) and toluene around 7.2 ppm and 2.3 ppm (×). The upfield spectrum portion from 6.3 to 8 ppm is magnified 10x to see the broad –N**H**$_3^+$ resonance.

Detailed ^{1}H NMR spectroscopy studies of metal-EDTA complexes from the literature offer a framework to analyze these results. A study from Gennaro and coworkers describes the geminal coupling of the methylene protons in the acetyl groups of an octahedral metal-EDTA complex.[44] With four unique methylene proton environments (in- and out-of-plane, axial and equatorial), the ^{1}H NMR spectrum should exhibit two AB quartet patterns. However, variable temperature studies show that the AB quartets coalesce upon heating. This is rationalized by one or both intramolecular rearrangement processes as follows: nitrogen inversion which results in exchange of the in- and out-of-plane acetyl groups, and Δ, Λ conversion where the acetyl groups rotate coordination spots on the metal so that the protons switch in- and out-of-plane as well as axial and equatorial environments (**Scheme 2a**).[45,46] The stoichiometry of the resulting octahedral indium EDTA complex requires four amines to deprotonate EDTA to form four equivalents of oleylammonium, then one charge balances the negatively charged indium EDTA octahedral complex and the other three form oleylammonium chloride salts (**Scheme 2b**). The shift of the amine proton signal from 2.9 ppm when oleylamine is coordinated to $InCl_3$ to a broad singlet around 7 ppm when EDTA is added supports the formation of oleylammonium (**Figure S12**).[39] These control experiments indicate that a tightly chelated octahedral indium EDTA complex forms in the initial reaction mixture containing $InCl_3$, EDTA, and oleylamine before the addition of the aminophosphine.

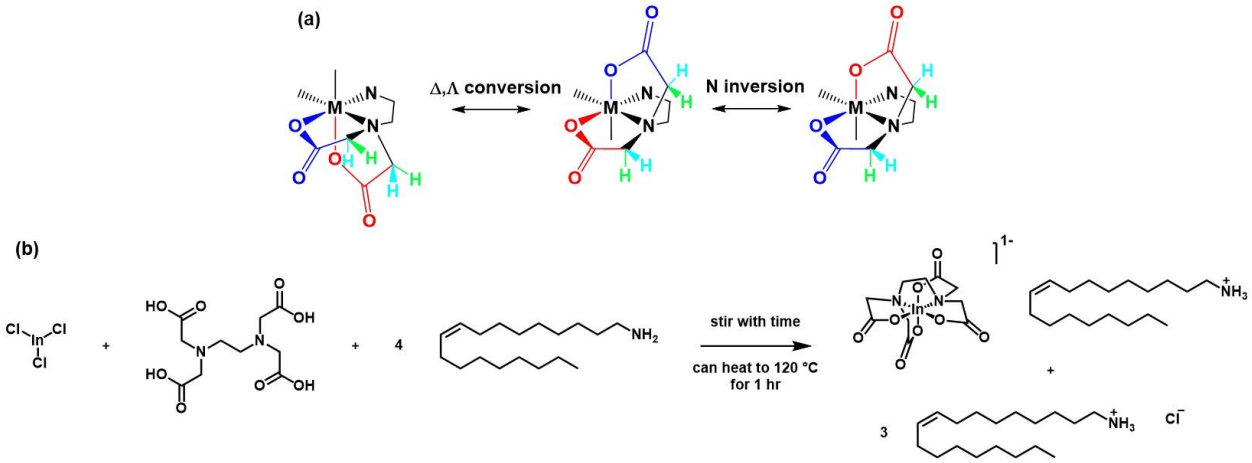

Scheme 2. (**a**) Demonstration of intramolecular rearrangement processes in an octahedral metal-EDTA complex that lead to coalescence of AB quartets in the ^{1}H NMR spectrum. In Δ, Λ conversion, the acetyl groups rotate coordination spots on the metal so the protons switch in-plane (blue) and out-of-plane (red), and axial (cyan) and equatorial (green) environments. Nitrogen inversion results in exchange of the in- and out-of-plane acetyl groups. (**b**) Proposed chemical equation for reaction mixture before addition of phosphorus.

Investigating the reactivity of the octahedral indium EDTA complex can give insights into how EDTA causes the size difference in the InP QD synthesis. First, the indium EDTA complex is stable through the initial degassing step of the synthesis, as seen through the retention of the characteristic AB quartet after heating for one hour at 120 °C (**Figure S10**). After heating at the QD synthesis temperature of 180 °C, the diagnostic AB quartet persists but is accompanied by the appearance of additional byproduct resonances and the formation of water (**Figure S10**). Therefore, without phosphorus present at the reaction temperature, the octahedral indium EDTA complex undergoes only partial decomposition evidenced by the AB quartet persistence and the amide/water formation.

With reasonable evidence suggesting that any EDTA added is chelating indium to form an octahedral complex at the time of phosphorus injection, it is important to determine the extent of reactivity with phosphorus of the chelated indium. When one equivalent of EDTA per indium is added to the InP QD synthesis to chelate all indium, UV-vis absorbance data shows an increase in broad, featureless absorption (**Figure S13a**) relative to the equivalent reaction run in the absence of aminophosphine (**Figure S14**). Despite the lack of clear InP QD formation with 1 equivalent of EDTA per indium, an initial rate can be extracted from the early reaction aliquot absorbance spectra and the result is slightly lower than the initial rate with 0.75 equivalents of EDTA per indium (**Figure S13b**). Taking into account the low reactivity of the chelated indium, the molecular cause of the EDTA-dependent size control can be identified. The initial rates of InP growth decrease slightly with lower indium concentrations (**Figure S9**), and the less reactive indium EDTA complex further decreases the initial InP growth rate leading to the drastic size decrease. This kinetically-informed competitive indium precursor system is summarized in **Scheme 3** as an explanation for the EDTA dose-dependent InP QD size decrease. The size

control is generalizable to other indium salts as InP QDs made using indium iodide instead of indium chloride also exhibit a size decrease with increasing equivalents of EDTA (**Figure S15**).

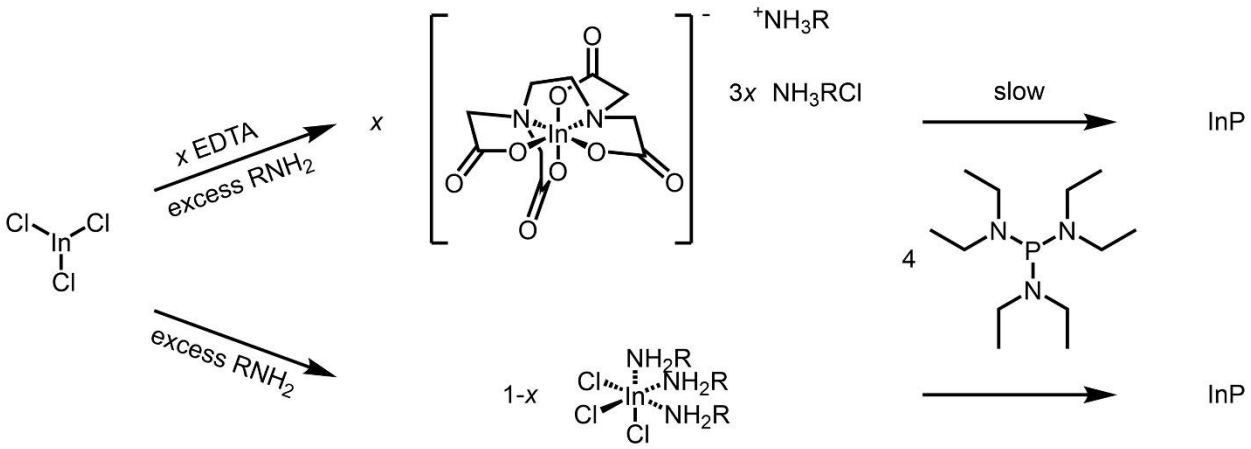

Scheme 3. Proposed reaction scheme showing the influence of EDTA chelation on indium precursor reactivity. Increasing equivalents of EDTA lowers the initial InP growth rate. (R = $C_{18}H_{35}$, x = 0, 0.25, 0.5, 0.75).

Conclusions

In conclusion, we have explored the effects of a multidentate ligand on indium precursor reactivity and the consequences for InP QD synthesis. The aminopolycarboxylic acid EDTA chelates indium in solution by forming an indium EDTA octahedral complex using the amine solvent as a deprotonation agent and source of charge compensating counter cations. Substoichiometric amounts of EDTA per indium allow zinc blende InP QDs with low polydispersity to be grown with a diameter range of 4.5 to 2.3 nm. We propose that the balance between free indium ($InCl_3$(oleylamine)$_3$)[34] and chelated indium ($In(EDTA)^-$) as precursors in solution causes the observed lower initial InP growth rates both because of the competitive sequestration of indium by EDTA and the lower reactivity of the indium EDTA complex. The unusual trend of smaller nanocrystals caused by lower initial growth rates is explained through the balance between nucleation and growth in a continuous nucleation scenario. The possibility of size control through surface stabilization effects was considered but discounted due to the lack of EDTA on the surface of purified QDs.

This study develops indium chelation as a synthetic handle in InP QD synthesis and shows a glimpse of the opportunities offered when metal cation reactivity and activity are controlled in QD synthesis. Analogues of synthetic control used in biomineralization, such as multidentate ligands, are sparsely used to control QD nucleation and growth but the unique regulation offered can overcome unresolved synthetic difficulties. For example, the non-ideal pre-nucleation clusters in PbS QDs were avoided by toggling lead ion reactivity using chelating ethers.[47] Continuing to apply insights from nature on QD synthesis through precise control over precursor coordination and reactivity will both expand our fundamental understanding of nucleation and growth processes and the commercial use of QDs through precise synthetic control.

Experimental Methods

General Practices. All glassware was dried in a 160 °C oven overnight prior to use. All syntheses were performed under an inert atmosphere of nitrogen using a glovebox or standard Schlenk techniques. Indium chloride (98%) and ethylenediaminetetraacetic acid (98.5%) were purchased from MilliporeSigma and dried before being stored in a nitrogen glovebox. Oleylamine (≥98%) was purchased from MilliporeSigma, dried over CaH_2, distilled, and stored over activated 3 Å molecular sieves in a nitrogen glovebox. Dimethylsulfoxide-d_6 (99.9%), benzene-d_6 (99.5%), and toluene-d_8 (99.5%) were purchased from Cambridge Isotope Laboratories and were similarly dried and stored. Anhydrous tris(diethyl)aminophosphine (97%) and anhydrous methanol (99.8%) were purchased from MilliporeSigma and used without further purification. Toluene (high-performance liquid chromatography grade) was purchased from Fisher and used as purchased for UV-vis absorbance spectroscopy of reaction aliquots. For QD purification, toluene was purchased from MilliporeSigma, collected from a solvent still, and stored over activated 3 Å molecular sieves in a nitrogen glovebox. UV-vis spectra were collected on a Cary 5000 spectrophotometer from Agilent.

Synthesis of InP QDs using $InCl_3$. Adapted from previously optimized conditions.[31] In a nitrogen glovebox, 0.3 mmol $InCl_3$, 0, 0.075, 0.15, 0.225, or 0.3 mmol EDTA, and 5 mL anhydrous oleylamine were added to a 50 mL 3-neck flask. On the Schlenk line, the solution was then placed under vacuum at 120 °C and degassed for 1 h. The vessel was then placed under an inert atmosphere and heated to 180 °C (unless alternate reaction temperature is specified). Once the reaction temperature was reached, 0.33 mL of tris(diethyl)aminophosphine (1.2 mmol) was rapidly injected. The reaction was monitored by UV-vis absorbance spectroscopy of 20 µL reaction aliquots in 2 mL toluene. The reaction was allowed to proceed until the absorbance spectrum remained constant, observed at 2 h, or allowed to react overnight with little change in the absorbance spectrum. The flask was then cooled down to room temperature before being moved into a nitrogen glovebox for purification. The QDs were precipitated with anhydrous methanol, centrifuged for 10 min at 7830 rpm, and resuspended in toluene. This procedure was repeated 3 times to remove excess oleylamine before additional sample analysis was performed (confirmed by ^{1}H NMR spectroscopy).

Synthesis of InP QDs using InI_3. InP QDs were synthesized using the same procedure as above but instead of 0.3 mmol $InCl_3$, 0.3 mmol of InI_3 was used, and the reaction was allowed to proceed until the absorbance spectrum remained constant, observed at 30 minutes.

Post-synthetic addition of EDTA to InP QDs. In a nitrogen glovebox, 0.15 mmol of EDTA was added to 0.6 mL anhydrous oleylamine to form a slurry. InP QDs with 0 equivalents of EDTA were synthesized according to the procedure above and after 2 hours of reaction, the EDTA-oleylamine slurry was injected into the reaction mixture. The reaction was monitored by UV-vis absorbance spectroscopy of 20 µL reaction aliquots in 2 mL toluene. The reaction was allowed to proceed until the absorbance spectrum remained constant, observed at 1 hour. The QDs were purified as described above before additional sample analysis.

^{1}H NMR Studies of $InCl_3$ and EDTA. In a nitrogen glovebox, 0.03 mmol $InCl_3$, 0.03 mmol of EDTA, 0.5 mL anhydrous DMSO-d_6, and 0.12 mmol anhydrous oleylamine were added to a 20 mL scintillation vial and stirred overnight to allow for homogeneous mixing. The solution was

transferred to an oven-dried airtight J. Young NMR tube and heated to 120 °C for 1 hour in a silicone oil bath, then 180 °C for 2 hours with removal for ^{1}H NMR spectroscopy as needed.

Transmission electron microscopy. All imaging was done on a FEI Tecnai G2 F20 SuperTwin microscope operated at 200 kV using bright field imaging. Samples were prepared in a nitrogen glovebox by drop-casting 5 μL of dilute QD suspensions in toluene onto a suspended ultrathin carbon film on a lacey carbon support film, 400 mesh, copper grids purchased from Ted Pella Inc, and allowed to dry fully (10 min) then placed under vacuum overnight. TEM size analysis was performed using manual analysis in ImageJ based off images from at least two different grid locations and over 300 particle diameter measurements per sample. Due to the low contrast of InP under the electron beam, standard deviation of diameter measurements may be artificially high.

Powder X-ray Diffraction. Powder XRD diffraction patterns were collected on solid films drop-cast onto a Si wafer using a Bruker D8 Discover diffractometer.

NMR spectroscopy. ^{1}H and ^{31}P NMR spectra were recorded on 500 MHz Bruker Advance spectrometers. ^{1}H NMR spectra were collected with 10 scans, 2 dummy scans, and a delay time of 30 s for QD samples or 10 s for samples of molecular indium and EDTA species. ^{31}P NMR spectra were collected with 135 scans and a delay time of 2 s for Figure S11 and 100 scans and a delay time of 10 s for Figure 5.

Supporting Information

Additional experimental details and supporting data including UV–vis absorbance spectra, TEM images, powder x-ray diffraction pattern fits, NMR and IR spectra, QD yields, initial rates, and discussion on determination of the lowest energy electronic transition, quantum dot size dispersity, product yield, and initial growth rate calculations.

Acknowledgements

This material is based upon work supported by the U.S. Department of Energy, Office of Science, Office of Basic Energy Sciences as part of the Energy Frontier Research Centers program: CSSAS-The Center for the Science of Synthesis Across Scales under award number DE-SC0019288. Part of this work was conducted at the Molecular Analysis Facility, a National Nanotechnology Coordinated Infrastructure (NNCI) site at the University of Washington with partial support from the National Science Foundation via awards NNCI-1542101 and NNCI-2025489. We also gratefully acknowledge Hao Nguyen for his work on the TOC graphic.

References

(1) Nudelman, F.; Sommerdijk, N. A. J. M. Biomineralization as an Inspiration for Materials Chemistry. *Angewandte Chemie International Edition* **2012**, *51* (27), 6582–6596. https://doi.org/10.1002/anie.201106715.

(2) Dorval Courchesne, N.-M.; Steiner, S. A.; Cantú, V. J.; Hammond, P. T.; Belcher, A. M. Biotemplated Silica and Silicon Materials as Building Blocks for Micro- to Nanostructures. *Chem. Mater.* **2015**, *27* (15), 5361–5370. https://doi.org/10.1021/acs.chemmater.5b01844.

(3) Nuraje, N.; Dang, X.; Qi, J.; Allen, M. A.; Lei, Y.; Belcher, A. M. Biotemplated Synthesis of Perovskite Nanomaterials for Solar Energy Conversion. *Advanced Materials* **2012**, *24* (21), 2885–2889. https://doi.org/10.1002/adma.201200114.
(4) Zhang, G.; Wei, S.; Belcher, A. M. Biotemplated Zinc Sulfide Nanofibers as Anode Materials for Sodium-Ion Batteries. *ACS Appl. Nano Mater.* **2018**, *1* (10), 5631–5639. https://doi.org/10.1021/acsanm.8b01254.
(5) Mao, C.; Flynn, C. E.; Hayhurst, A.; Sweeney, R.; Qi, J.; Georgiou, G.; Iverson, B.; Belcher, A. M. Viral Assembly of Oriented Quantum Dot Nanowires. *PNAS* **2003**, *100* (12), 6946–6951. https://doi.org/10.1073/pnas.0832310100.
(6) Braun, P. V.; Osenar, P.; Stupp, S. I. Semiconducting Superlattices Templated by Molecular Assemblies. *Nature* **1996**, *380* (6572), 325–328. https://doi.org/10.1038/380325a0.
(7) Monahan, M.; Cai, B.; Jian, T.; Zhang, S.; Zhu, G.; Chen, C.-L.; Yoreo, J. J. D.; Cossairt, B. M. Peptoid-Directed Assembly of CdSe Nanoparticles. *Nanoscale* **2021**, *13* (2), 1273–1282. https://doi.org/10.1039/D0NR07509D.
(8) Klug, M. T.; Dorval Courchesne, N.-M.; Lee, Y. E.; Yun, D. S.; Qi, J.; Heldman, N. C.; Hammond, P. T.; Fang, N. X.; Belcher, A. M. Mediated Growth of Zinc Chalcogen Shells on Gold Nanoparticles by Free-Base Amino Acids. *Chem. Mater.* **2017**, *29* (16), 6993–7001. https://doi.org/10.1021/acs.chemmater.7b02571.
(9) Singh, S.; Bozhilov, K.; Mulchandani, A.; Myung, N.; Chen, W. Biologically Programmed Synthesis of Core-Shell CdSe/ZnS Nanocrystals. *Chem. Commun.* **2010**, *46* (9), 1473–1475. https://doi.org/10.1039/B920688D.
(10) Qi, X.; Jin, B.; Cai, B.; Yan, F.; Yoreo, J. D.; Chen, C.-L.; Pfaendtner, J. Molecular Driving Force for Facet Selectivity of Sequence-Defined Amphiphilic Peptoids at Au–Water Interfaces. *J. Phys. Chem. B* **2022**, *126* (27), 5117-5126. https://pubs.acs.org/doi/10.1021/acs.jpcb.2c02638.
(11) Hellner, B.; Stegmann, A. E.; Pushpavanam, K.; Bailey, M. J.; Baneyx, F. Phase Control of Nanocrystalline Inclusions in Bioprecipitated Titania with a Panel of Mutant Silica-Binding Proteins. *Langmuir* **2020**, *36* (29), 8503–8510. https://doi.org/10.1021/acs.langmuir.0c01108.
(12) Yan, F.; Liu, L.; Walsh, T. R.; Gong, Y.; El-Khoury, P. Z.; Zhang, Y.; Zhu, Z.; De Yoreo, J. J.; Engelhard, M. H.; Zhang, X.; Chen, C.-L. Controlled Synthesis of Highly-Branched Plasmonic Gold Nanoparticles through Peptoid Engineering. *Nat Commun* **2018**, *9* (1), 2327. https://doi.org/10.1038/s41467-018-04789-2.
(13) Wadas, T. J.; Wong, E. H.; Weisman, G. R.; Anderson, C. J. Coordinating Radiometals of Copper, Gallium, Indium, Yttrium, and Zirconium for PET and SPECT Imaging of Disease. *Chem. Rev.* **2010**, *110* (5), 2858–2902. https://doi.org/10.1021/cr900325h.
(14) Sugimoto, T.; Dirige, G. E.; Muramatsu, A. Formation Mechanism of Monodisperse CdS Particles from Concentrated Solutions of Cd–EDTA Complexes. *Journal of Colloid and Interface Science* **1996**, *182* (2), 444–456. https://doi.org/10.1006/jcis.1996.0486.
(15) Zhou, L.; Wang, S.; Ma, H.; Ma, S.; Xu, D.; Guo, Y. Size-Controlled Synthesis of Copper Nanoparticles in Supercritical Water. *Chemical Engineering Research and Design* **2015**, *98*, 36–43. https://doi.org/10.1016/j.cherd.2015.04.004.
(16) Deki, S.; Kuratani, K.; Uemura, M.; Akamatsu, K.; Mizuhata, M.; Kajinami, A. Aqueous Solution-Based Synthesis of Rare Earth-Doped Metal Oxide Thin Films. *Thin Solid Films* **2004**, *460* (1), 83–86. https://doi.org/10.1016/j.tsf.2004.01.077.

(17) Wang, R.; Liu, C.; Zeng, J.; Li, K.; Wang, H. Fabrication and Morphology Control of BaWO4 Thin Films by Microwave Assisted Chemical Bath Deposition. *Journal of Solid State Chemistry* **2009**, *182* (4), 677–684. https://doi.org/10.1016/j.jssc.2008.12.014.
(18) Wang, Z.; Tao, F.; Yao, L.; Cai, W.; Li, X. Selected Synthesis of Cubic and Hexagonal NaYF4 Crystals via a Complex-Assisted Hydrothermal Route. *Journal of Crystal Growth* **2006**, *290* (1), 296–300. https://doi.org/10.1016/j.jcrysgro.2006.01.012.
(19) Yao, S.; Qi, M.; Qi, L.; Ding, Y.; Chen, M.; Wang, Y. Investigation of EDTA Concentration on the Size of Carbonated Flowerlike Hydroxyapatite Microspheres. *Royal Society Open Science 8* (3), 202148. https://doi.org/10.1098/rsos.202148.
(20) Susman, M. D.; Feldman, Y.; Vaskevich, A.; Rubinstein, I. Chemical Deposition of Cu2O Nanocrystals with Precise Morphology Control. *ACS Nano* **2014**, *8* (1), 162–174. https://doi.org/10.1021/nn405891g.
(21) Ding, M.; Yin, S.; Ni, Y.; Lu, C.; Chen, D.; Zhong, J.; Ji, Z.; Xu, Z. Controlled Synthesis of β-NaYF4:Yb3+/Er3+ Microstructures with Morphology- and Size-Dependent Upconversion Luminescence. *Ceramics International* **2015**, *41* (6), 7411–7420. https://doi.org/10.1016/j.ceramint.2015.02.054.
(22) Li, C.; Quan, Z.; Yang, J.; Yang, P.; Lin, J. Highly Uniform and Monodisperse β-NaYF4:Ln3+ (Ln = Eu, Tb, Yb/Er, and Yb/Tm) Hexagonal Microprism Crystals: Hydrothermal Synthesis and Luminescent Properties. *Inorg. Chem.* **2007**, *46* (16), 6329–6337. https://doi.org/10.1021/ic070335i.
(23) Hamachi, L. S.; Jen-La Plante, I.; Coryell, A. C.; De Roo, J.; Owen, J. S. Kinetic Control over CdS Nanocrystal Nucleation Using a Library of Thiocarbonates, Thiocarbamates, and Thioureas. *Chem. Mater.* **2017**, *29* (20), 8711–8719. https://doi.org/10.1021/acs.chemmater.7b02861.
(24) Sugimoto, T. Underlying Mechanisms in Size Control of Uniform Nanoparticles. *Journal of Colloid and Interface Science* **2007**, *309* (1), 106–118. https://doi.org/10.1016/j.jcis.2007.01.036.
(25) Gary, D. C.; Glassy, B. A.; Cossairt, B. M. Investigation of Indium Phosphide Quantum Dot Nucleation and Growth Utilizing Triarylsilylphosphine Precursors. *Chem. Mater.* **2014**, *26* (4), 1734–1744. https://doi.org/10.1021/cm500102q.
(26) Cossairt, B. M. Shining Light on Indium Phosphide Quantum Dots: Understanding the Interplay among Precursor Conversion, Nucleation, and Growth. *Chem. Mater.* **2016**, *28* (20), 7181–7189. https://doi.org/10.1021/acs.chemmater.6b03408.
(27) Tamang, S.; Lincheneau, C.; Hermans, Y.; Jeong, S.; Reiss, P. Chemistry of InP Nanocrystal Syntheses. *Chem. Mater.* **2016**, *28* (8), 2491–2506. https://doi.org/10.1021/acs.chemmater.5b05044.
(28) Kim, J. Y.; Steeves, A. H.; Kulik, H. J. Harnessing Organic Ligand Libraries for First-Principles Inorganic Discovery: Indium Phosphide Quantum Dot Precursor Design Strategies. *Chem. Mater.* **2017**, *29* (8), 3632–3643. https://doi.org/10.1021/acs.chemmater.7b00472.
(29) Li, Y.; Hou, X.; Shen, Y.; Dai, N.; Peng, X. Tuning the Reactivity of Indium Alkanoates by Tertiary Organophosphines for the Synthesis of Indium-Based Quantum Dots. *Chem. Mater.* **2021**. https://doi.org/10.1021/acs.chemmater.1c03219.
(30) Tessier, M. D.; Dupont, D.; De Nolf, K.; De Roo, J.; Hens, Z. Economic and Size-Tunable Synthesis of InP/ZnE (E = S, Se) Colloidal Quantum Dots. *Chem. Mater.* **2015**, *27* (13), 4893–4898. https://doi.org/10.1021/acs.chemmater.5b02138.

(31) Buffard, A.; Dreyfuss, S.; Nadal, B.; Heuclin, H.; Xu, X.; Patriarche, G.; Mézailles, N.; Dubertret, B. Mechanistic Insight and Optimization of InP Nanocrystals Synthesized with Aminophosphines. *Chem. Mater.* **2016**, *28* (16), 5925–5934. https://doi.org/10.1021/acs.chemmater.6b02456.
(32) McMurtry, B. M.; Qian, K.; Teglasi, J. K.; Swarnakar, A. K.; De Roo, J.; Owen, J. S. Continuous Nucleation and Size Dependent Growth Kinetics of Indium Phosphide Nanocrystals. *Chem. Mater.* **2020**, *32* (10), 4358–4368. https://doi.org/10.1021/acs.chemmater.0c01561.
(33) Valleix, R.; Cisnetti, F.; Okuno, H.; Boutinaud, P.; Chadeyron, G.; Boyer, D. Size-Controlled Indium Phosphide Quantum Dots for Bright and Tunable Light Emission by Simple Hindered Diamine Addition. *ACS Appl. Nano Mater.* **2021**, *4* (10), 11105–11114. https://doi.org/10.1021/acsanm.1c02577.
(34) Laufersky, G.; Bradley, S.; Frécaut, E.; Lein, M.; Nann, T. Unraveling Aminophosphine Redox Mechanisms for Glovebox-Free InP Quantum Dot Syntheses. *Nanoscale* **2018**, *10* (18), 8752–8762. https://doi.org/10.1039/C8NR01286E.
(35) Chen, J.; Gao, J.; Wang, X. Thermal Decomposition of Ethylenediaminetetraacetic Acid in the Presence of 1,2-Phenylenediamine and Hydrochloric Acid. *J. Braz. Chem. Soc.* **2006**, *17*, 880–885. https://doi.org/10.1590/S0103-50532006000500010.
(36) Kim, K.; Yoo, D.; Choi, H.; Tamang, S.; Ko, J.-H.; Kim, S.; Kim, Y.-H.; Jeong, S. Halide–Amine Co-Passivated Indium Phosphide Colloidal Quantum Dots in Tetrahedral Shape. *Angewandte Chemie* **2016**, *128* (11), 3778–3782. https://doi.org/10.1002/ange.201600289.
(37) Holder, C. F.; Schaak, R. E. Tutorial on Powder X-Ray Diffraction for Characterizing Nanoscale Materials. *ACS Nano* **2019**, *13* (7), 7359–7365. https://doi.org/10.1021/acsnano.9b05157.
(38) Calvin, J. J.; Kaufman, T. M.; Sedlak, A. B.; Crook, M. F.; Alivisatos, A. P. Observation of Ordered Organic Capping Ligands on Semiconducting Quantum Dots via Powder X-Ray Diffraction. *Nat Commun* **2021**, *12* (1), 2663. https://doi.org/10.1038/s41467-021-22947-x.
(39) Dümbgen, K. C.; Leemans, J.; De Roo, V.; Minjauw, M.; Detavernier, C.; Hens, Z. Surface Chemistry of InP Quantum Dots, Amine–Halide Co-Passivation, and Binding of Z-Type Ligands. *Chem. Mater.* **2023**. https://doi.org/10.1021/acs.chemmater.2c02960.
(40) De Roo, J.; Yazdani, N.; Drijvers, E.; Lauria, A.; Maes, J.; Owen, J. S.; Van Driessche, I.; Niederberger, M.; Wood, V.; Martins, J. C.; Infante, I.; Hens, Z. Probing Solvent–Ligand Interactions in Colloidal Nanocrystals by the NMR Line Broadening. *Chem. Mater.* **2018**, *30* (15), 5485–5492. https://doi.org/10.1021/acs.chemmater.8b02523.
(41) Chen, M.; Feng, Y.-G.; Wang, X.; Li, T.-C.; Zhang, J.-Y.; Qian, D.-J. Silver Nanoparticles Capped by Oleylamine: Formation, Growth, and Self-Organization. *Langmuir* **2007**, *23* (10), 5296–5304. https://doi.org/10.1021/la700553d.
(42) Tessier, M. D.; De Nolf, K.; Dupont, D.; Sinnaeve, D.; De Roo, J.; Hens, Z. Aminophosphines: A Double Role in the Synthesis of Colloidal Indium Phosphide Quantum Dots. *J. Am. Chem. Soc.* **2016**, *138* (18), 5923–5929. https://doi.org/10.1021/jacs.6b01254.
(43) Kenny, N. P.; Rajendran, K. V.; Jennings, E. V.; Gilheany, D. G. Cleavage of P□O in the Presence of P–N: Aminophosphine Oxide Reduction with In Situ Boronation of the PIII Product. *Chemistry – A European Journal* **2013**, *19* (42), 14210–14214. https://doi.org/10.1002/chem.201302907.

(44) Gennaro, M. C.; Mirti, P.; Casalino, C. NMR Study of Intramolecular Processes in EDTA Metal Complexes. *Polyhedron* **1983**, *2* (1), 13–18. https://doi.org/10.1016/S0277-5387(00)88025-0.
(45) Ba, Y.; Han, S.; Ni, L.; Su, T.; Garcia, A. Dynamic NMR of Intramolecular Exchange Processes in EDTA Complexes of Sc3+, Y3+, and La3+. *J. Chem. Educ.* **2006**, *83* (2), 296. https://doi.org/10.1021/ed083p296.
(46) Han, S.; Ba, Y. Determination of the Concentrations of Metal Cations in Aqueous Solutions Using Proton NMR Spectral Area Integration of the EDTA Complexes. *Journal of Solution Chemistry* **2004**, *33* (3), 301–312. https://doi.org/10.1023/B:JOSL.0000035362.27111.54.
(47) Green, P. B.; Wang, Z.; Sohn, P.; Imperiale, C. J.; Voznyy, O.; Wilson, M. W. B. Glycol Ether Additives Control the Size of PbS Nanocrystals at Reaction Completion. *J. Mater. Chem. C* **2020**, *8* (35), 12068–12074. https://doi.org/10.1039/D0TC03252B.

TOC Graphic